Biomedical Signal Processing and Control 98 (2024) 106759

Contents lists available at ScienceDirect

Biomedical Signal Processing and Control

journal homepage: www.elsevier.com/locate/bspc

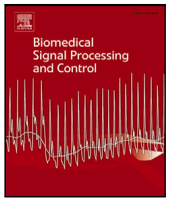

Exploring the dynamic relationship: Changes in photoplethysmography features corresponding to intracranial pressure variations

George R.E. Bradley *, Panicos A. Kyriacou

Research Centre for Biomedical Engineering, City, University of London, UK

ARTICLE INFO

Keywords:
Signal processing
Traumatic brain injury
Intracranial pressure
Photoplethysmography

ABSTRACT

This study investigates the relationship between photoplethysmography (PPG) signals and intracranial pressure (ICP) through two primary hypotheses. Firstly, it examines whether alterations in PPG-derived features correspond to changes in ICP levels. Secondly, it explores whether these changes are more pronounced in features derived from "cerebral" long-distance near-infrared (NIR) PPG data compared to "extracerebral" short-distance NIR-PPG data. A clinical dataset comprising synchronised measurements from a non-invasive NIR-PPG sensor and an intra-parenchymal, invasive ICP pressure probe across 27 patients was compiled. From this dataset, two distinct datasets were derived, comprising short and long-distance NIR-PPG data. Within each dataset, 141 features were extracted for every one-minute window of non-invasive NIR-PPG data, including original, first derivative, and second derivative features. Correlation analysis using Spearman's correlation and a non-parametric Kruskal–Wallis test across the range of ICP values were conducted to evaluate the relationship between features and ICP levels. The results support both hypotheses, showing significant correlations between the features and ICP levels. Specifically, 77.30% and 79.43% of features significantly correlated ($p < 0.05$) with the label in distal and proximal datasets, respectively. Kruskal–Wallis analysis revealed that 81.56% and 75.89% of features significantly changed ($p < 0.05$) across ICP groups 0–10, 10–20, and 20–39 mmHg. The distal dataset yielded a meaningfully higher absolute average correlation coefficient of all features and significantly correlated features in-comparison to the proximal dataset of 25.76% and 24.24% respectively. These findings indicate NIR-PPG features are reflective of variations in ICP.

1. Introduction

1.1. Cerebral hemodynamics and photoplethysmography changes

Cerebral perfusion pressure (CPP) and cerebral blood flow (CBF) are central in understanding the dynamics of blood flow within the brain's vascular system. CPP is the gradient between mean arterial pressure (MAP) and intracranial pressure (ICP), expressed in millimeters of mercury (mmHg). CPP is fundamental for facilitating blood flow to the brain. Normal CPP values range from 60 to 100 mmHg, maintaining adequate cerebral blood flow and ensuring brain health [1].

CBF represents the volume of blood flowing through a given amount of brain tissue over time, measured in milliliters per 100 grams of brain tissue per minute (ml/100g/min). Cerebral autoregulation plays a key role in maintaining CBF by adjusting cerebral vascular resistance to ensure consistent blood flow despite variations in CPP, within the autoregulatory limits of approximately 50 to 150 mmHg. When CPP falls outside of these bounds, CBF becomes directly proportionate to CPP, elevating the risk of ischemia or hyperemia due to diminished or excessive blood flow to the brain [1].

ICP is the pressure within the cranial vault, governed by the Monro-Kellie hypothesis, which posits that the cranial compartment's volume is fixed, comprising brain tissue, cerebral blood, and cerebrospinal fluid (CSF) [2]. Variations in ICP arise from changes in these components due to pathological conditions such as mass lesions, venous sinus obstructions, and cerebral edema. Fig. 1 illustrates the progressive relationship between the increase in volume of the intracranial pathologies within the cranial vault (depicted in red) which can be caused by TBI and the corresponding rise in ICP.

These changes can trigger compensatory mechanisms aimed at preserving normal ICP levels, which are typically between 10 to 15 mmHg in adults and 3 to 7 mmHg in children [3].

Elevation in ICP can reduce CPP by increasing the resistance against arterial blood entering the brain. This elevation in ICP and consequential reduction in CPP triggers cerebral autoregulation, which adjusts the diameter of cerebral vessels, vasodilation to increase blood flow when CPP is low and vasoconstriction to decrease flow when CPP is high. However, elevated ICP and the subsequent increase in pressure

* Corresponding author.
E-mail address: george.bradley@city.ac.uk (G.R.E. Bradley).

https://doi.org/10.1016/j.bspc.2024.106759
Received 30 April 2024; Received in revised form 22 July 2024; Accepted 8 August 2024
Available online 23 August 2024

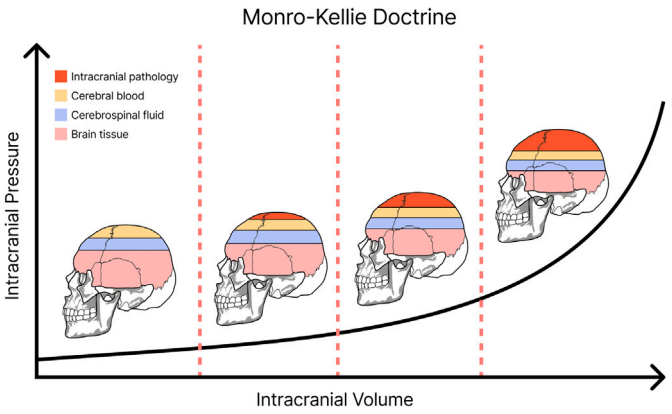

Fig. 1. Illustration of the relationship between increasing intracranial pathologies and consequential increases in intracranial pressure. The four skull images represent different stages of volume increase within the cranial compartments due to the increasing volume of intracranial pathologies mirrored by a subsequent increase in intracranial pressure.

exerted on the cerebral vessels can lead to a decrease in cerebral compliance characterised by the vessels' diminished ability to deform which can cause cerebral dysregulation where blood vessels cannot dilate sufficiently to counter reduced CPP, leading to a sustained drop in CBF.

Photoplethysmography (PPG) is a non-invasive optical technique that detects blood volume changes with each cardiac cycle based upon the absoptivity of light. The pulsatility of the PPG signal, reflecting these blood volume changes, varies between systolic and diastolic phases of the cardiac cycle. The systolic increase in blood volume results in increased absorbance of light in tissue compared to the diastolic state. This relative change in light absorbance gives rise to the PPG pulsatile waveform synchronous with each heartbeat [4,5]. Given the influence of ICP on CPP, and cerebral autoregulatory mechanisms, we posit that increases in ICP, and the suspected changes in flow dynamics as a consequence of variations in the mechanistic properties of vessels coupled with the expected decrease in cerebral blood volume stemming from cerebral dysregulation, diminished CPP, and CBF alongside resultant variations in light absorbance, will manifest in identifiable changes to PPG waveform morphology.

1.2. Current state of cardiac waveform based ICP monitoring

A growing body of research is exploring methods that leverage cardiac waveforms, such as diffuse correlation spectroscopy (DCS) and near-infrared spectroscopy (NIRS), for the non-invasive estimation of ICP.

An initial study in 1997 revealed that NIRS readings were significantly reduced when ICP exceeded 25 mmHg compared to when it was below this threshold, indicating the utility of NIRS in assessing elevated ICP [6]. Further investigations by Ruesch et al. focused on non-invasively measuring ICP in non-human primates using NIRS [7], where NIRS measurements were taken under various induced ICP levels. This research demonstrated a strong correlation between hemoglobin levels and induced ICP, thereby suggesting NIRS's capability for non-invasive ICP monitoring. In subsequent research, Ruesch et al. utilised both morphological and time series features from DCS pulsations along with MAP to predict ICP non-invasively [8], achieving a Coefficient of determination (R^2) of 0.92 and a mean squared error (MSE) of 3.3 mmHg. This group expanded their work by investigating features from NIRS-derived cardiac waveforms with MAP for ICP estimation [9], which improved the R^2 to 0.937 and reduced the MSE to 2.703 mmHg. Further studies have also shown the potential of using PPG waveform features to correlate with ICP levels, with findings indicating a R^2 of 0.66 [10].

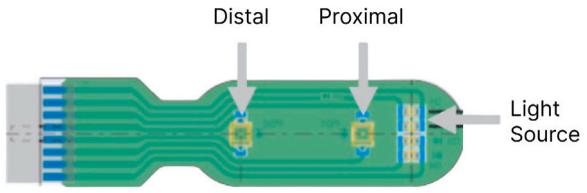

Fig. 2. A diagram showcasing the design of the non-invasive intracranial pressure "nICP" sensor, highlighting the placement of the photodiodes and the light source.

A healthy volunteers study investigated the use of pulsatile NIRS signals to detect changes in ICP in healthy volunteers. The results revealed significant differences in the features extracted from these signals, demonstrating a correlation with ICP changes induced by positional changes and Valsalva manoeuvres [11]. This research suggests the promising utility of PPG waveform features as a potential avenue for non-invasive ICP measurement.

This study contributes to the growing body of research associated with the relationship between cardiac waveform morphology and ICP monitoring. We provide statistical findings using clinically collected, labelled data to provide evidence of a dynamic relationship between changes in cardiac waveform morphology and variations in ICP.

2. Materials and methods

2.1. Non-invasive sensor

This research is based upon data produced by an in-house, NIRS, reflectance, non-invasive optical ICP sensor, hereinafter referred to as the "nICP" sensor [12]. The nICP sensor consists of four LEDs at four different wavelengths (770, 810, 855 and 880 nm) and two photodiodes "*proximal*" and "*distal*" positioned at 10 mm and 35 mm from the light source representing short-distance and long-distance NIRS data respectively. The sensor is arranged as shown in Fig. 2.

Findings from a montecarlo simulation of the light-tissue interaction propose that the data from the proximal photodiode corresponds to extracerebral data, while the data from the distal photodiode represents a combination of extracerebral and cerebral data [13].

Fig. 3 shows the indicative placement of the non-invasive nICP sensor (indicated by a green arrow) and the invasive sensor (indicated by a red arrow) on a patient. The nICP sensor is positioned on the patient's forehead, below the hairline.

2.2. Data

The primary dataset consists of data from 40 patients with severe traumatic brain injury (TBI) recruited from the intensive therapy unit (ITU) of the Royal London Hospital. The non-randomised data collection was performed between January 2020 and July 2021 (ClinicalTrials No. NCT05632302). Each patient had an implanted invasive ICP probe (Raumedic® Neurovent-P intra-parenchymal pressure probe) and approximately 5 h after admission the nICP sensor was affixed to the patient's forehead below the hairline. The non-invasive and invasive data were collected synchronously. The patients' average age was 43.92 years, with a male-to-female ratio of 7:1 (35 male, 5 female). Severe TBI diagnoses were determined using the guidelines from the Fourth Edition of the Management of Severe Traumatic Brain Injury [14]. Potential participants were excluded if they were considered unlikely to survive for 48 h or if a personal consultee advised against their participation. Patients who had undergone decompressive craniectomy were also excluded due to poor signal quality caused by the damping effect of the surgery.

Data collection lasted for an average of 42.16 h. None of the patients received external ventricular drainage. If a patient was taken out of

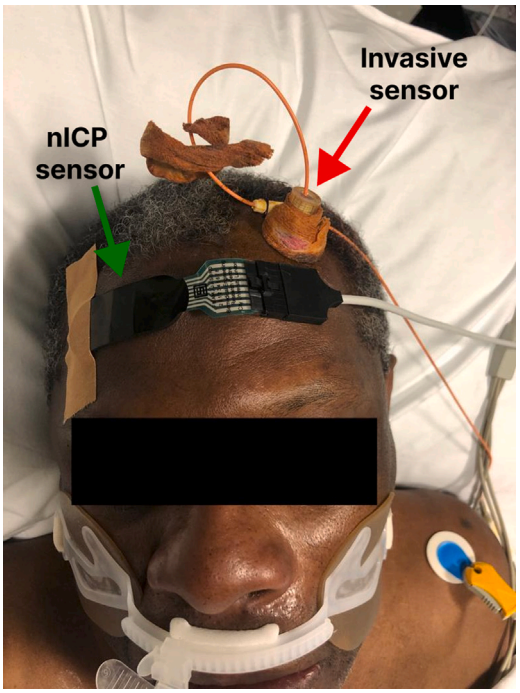

Fig. 3. An image depicting the indicative placement of the non-invasive nICP sensor (indicated by a green arrow) and the invasive sensor (indicated by a red arrow) on a patient.

the ITU for a scan, surgery or other intervention, the nICP sensor was detached and left in situ. Upon the patient's return to the ITU, both the nICP sensor and the invasive monitor were reconnected, and data collection resumed. In no cases was the invasive pressure probe removed or re-implanted.

This research focuses on the optical signals from the 810 nm wavelength at both proximal and distal photodiodes. The selection of the 810 nm wavelength is based on the property that oxyhemoglobin and deoxyhemoglobin exhibit the same absorption characteristics at this wavelength, enabling the extraction of an optical signal independent of blood oxygenation and eliminating it as a confounding factor [15]. The nICP monitor was calibrated for each patient through the adjustment of the LED intensity and amplification gain. Calibration was performed before recording started. The data was sampled at a frequency of 100 Hz. We refer to the nICP data as "NIR-PPG".

2.3. Data preprocessing

2.3.1. Denoising

Initially, the dataset consisted of data from 40 patients. Of these 40, the data of 6 patients were identified as either being corrupted or missing information resulting in a dataset of 34 patients. Of these, following visual inspection, the data of 7 patients were removed due to either (i) sustained poor quality, pulsatile, NIR-PPG data or (ii) suspected erroneous ICP data. Resulting in a final dataset from 27 patients.

Prior to the denoising of the dataset, an additional step was taken in order to handle erroneous ICP values. The assumption was made that values of ICP $\geq$ 60 mmHg or $<$ 0 mmHg, could be erroneous or biologically implausible. Consequently, these instances were removed from both the ICP and NIR-PPG data. Values above 60 mmHg may indicate potential measurement errors, while negative values are physiologically implausible. Fig. 4 depicts an example of recorded ICP with erroneous data points both above 60 mmHg and below 0 mmHg. In cases which Fig. 5 illustrates were there are sustained ICP values outside of the biologically feasible bounds it seemed reasonable to assume there was a invasive measurement error and subsequently the data of these patient's was excluded.

Within the dataset, two main sources of noise are hypothesised to be present (i) motion artifacts, which are identified by irregular signal morphology or high amplitude variance, and (ii) photodetector saturation, characterised by areas with little or no amplitude variance referred to as "flat lines". Fig. 6 shows an example of the noise within the data. The non-invasive data were denoised utilising the *Envelope PPG Denoising Algorithm* [16]. Any instances of data identified as anomalous were removed from both the NIR-PPG data and the reference ICP data to ensure temporal synchronicity between the datasets. After denoising, a visual inspection of the NIR-PPG data for each patient was performed. Data from patients with consistently poor signal quality were excluded.

2.3.2. Data selection protocol

To effectively evaluate our hypotheses, we refined the denoised dataset to only include high-quality pulsatile data for statistical analysis, a procedure we termed the "6 h protocol". As outlined in section 2.4, we performed feature extraction on 1-minute windows of data, we therefore oriented our data selection around this window size. We developed a "window selector" tool in Python using Tkinter, enabling the inspection of patient data in 1-minute windows to categorise each as either "good" or "bad" quality, with instances classified as "good" being recorded. Fig. 7 illustrates the *window selector* interface. This selection process entailed commencing at the beginning of the recording and labelling 6 h of data per patient as "good", or using all available "good" data if less than 6 h were classified as "good". ICP changes tend to occur gradually over time due to the slow adaptation of the brain's compartments to alterations in volume and pressure [17]. The period of 6 h was deemed a reasonable duration which would encompass the natural fluctuations and trends in ICP. This assessment was conducted by the same person across all patients using the distal NIR-PPG data, with the identified "good" instances subsequently being extracted from the both proximal and reference datasets to ensure temporal synchronicity. Although arifacts were present in both the proximal and distal data, the distal data consistently exhibited more severe artifacts during these periods. Therefore, the distal data was selected as the primary reference for guiding data labelling.

2.3.3. Data normalisation

Each one minute window of data was processed in order to remove baseline wandering and to scale the data to enhance inter patient comparison and aid in the creation of a shared distribution.

In order to attempt to diminish the possible effect of calibration on the data collected from multiple patients the alternating current (AC) and direct current (DC) components of each patient's signal data were isolated using a bandpass and lowpass filter respectively. The bandpass frequency band ranged from 0.4 to 10 Hz, the low pass cutoff frequency was set to 0.4 Hz. By dividing the AC component of the signal by the DC component this aimed to minimise the effects of the patient level calibration and provide a representation of the signal that is less influenced by calibration variations and baseline wandering allowing for more reliable feature extraction.

Following the AC/DC processing, each window's data were normalised to a range of (0,1) to account for inter-patient amplitudinal variance and to aid in the creation of a shared distribution across patients in the feature space.

2.4. Feature engineering

The NIR-PPG dataset was segmented into 1-minute windows, with the median ICP value over each window being used as a label. This 1-minute window size was chosen considering the possible clinical relevance and practicality of the prediction frequency. Longer window

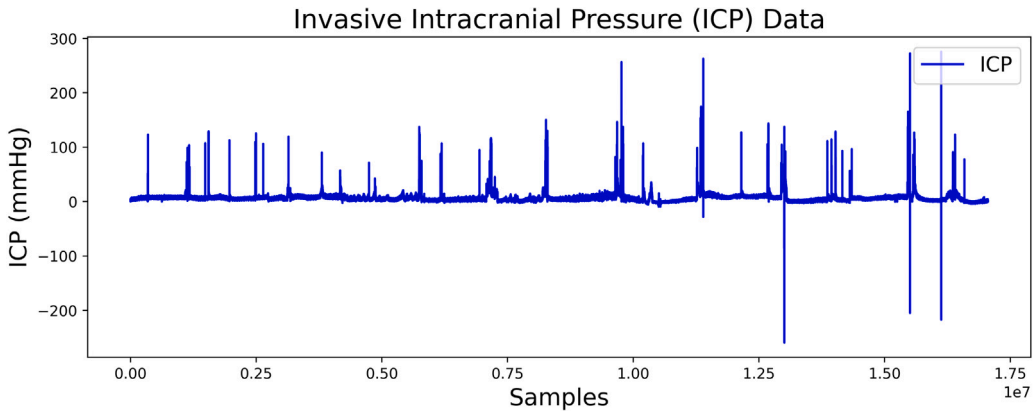

Fig. 4. A figure depicting the invasive intracranial pressure data recorded from a patient which includes assumed erroneous values above 60 mmHg and below 0 mmHg.

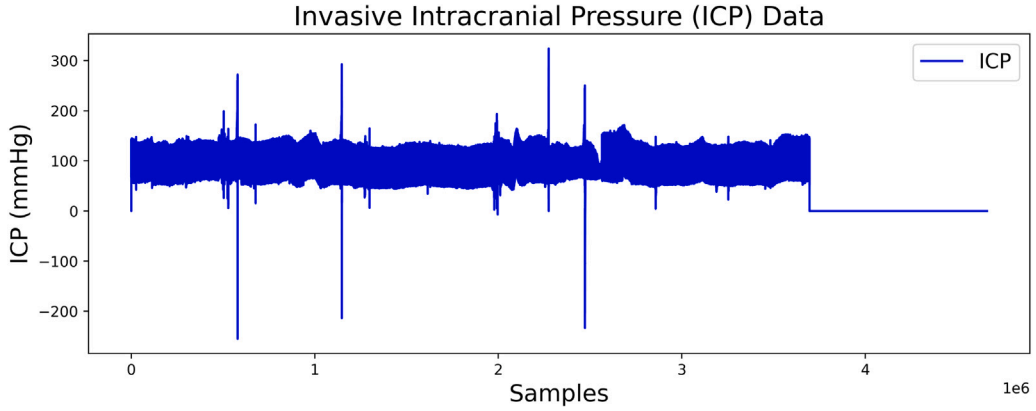

Fig. 5. A figure depicting the invasive intracranial pressure data recorded from a patient which includes assumed erroneous elevated values with a mean ≥ 60 mmHg.

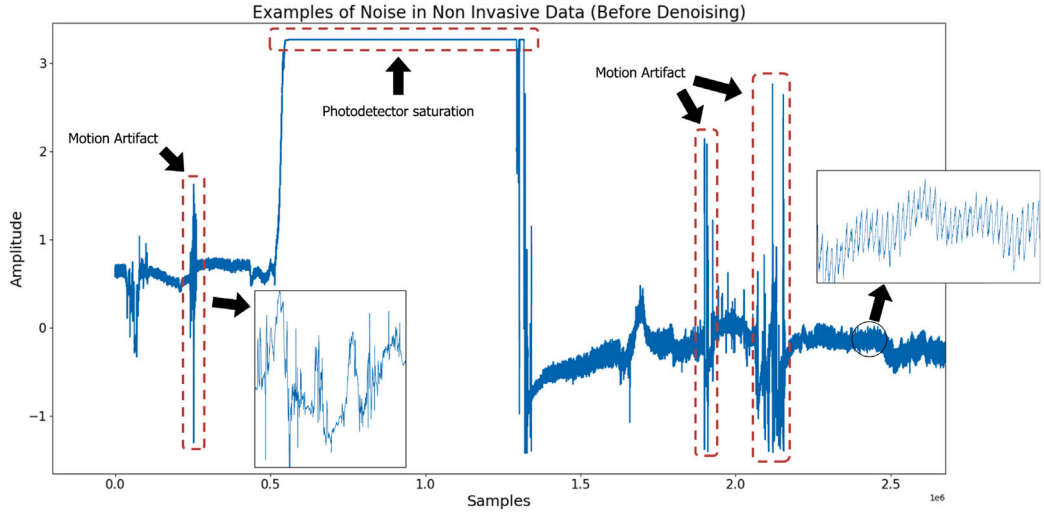

Fig. 6. Distal signal data with highlighted noise attributed to motion artifact and photodetector saturation. Visual aids emphasise the presence of noise within the window.

durations might be less favourable in a clinical setting, and our goal was to use a window size that maximises the amount of relevant data available for prediction while still being clinically manageable. The extracted features are derived from the AC, pulsatile component of the signal. In order to capture as much of the morphology of the signal, which is linked to hemodynamic changes, for each window of data 141 morphological and time-series features were extracted across the original signal and its first and second derivatives as shown in Table 3 in the appendix. Figs. 8 and 9 depict the primary time series and morphological features extracted from the cardiac pulses. The feature representation for each window was determined by computing the median of each feature across all pulses within that window. The derivatives of the signal were calculated using a Savitzky-Golay filter using a polynomial of 7 and a window size of 101.

The pulse detection algorithm used is predicated upon the crossing points of the signal and the moving average of the signal. The general concept of the algorithm is, if the mean of the data between crossing points is greater than the mean of the moving average between crossing

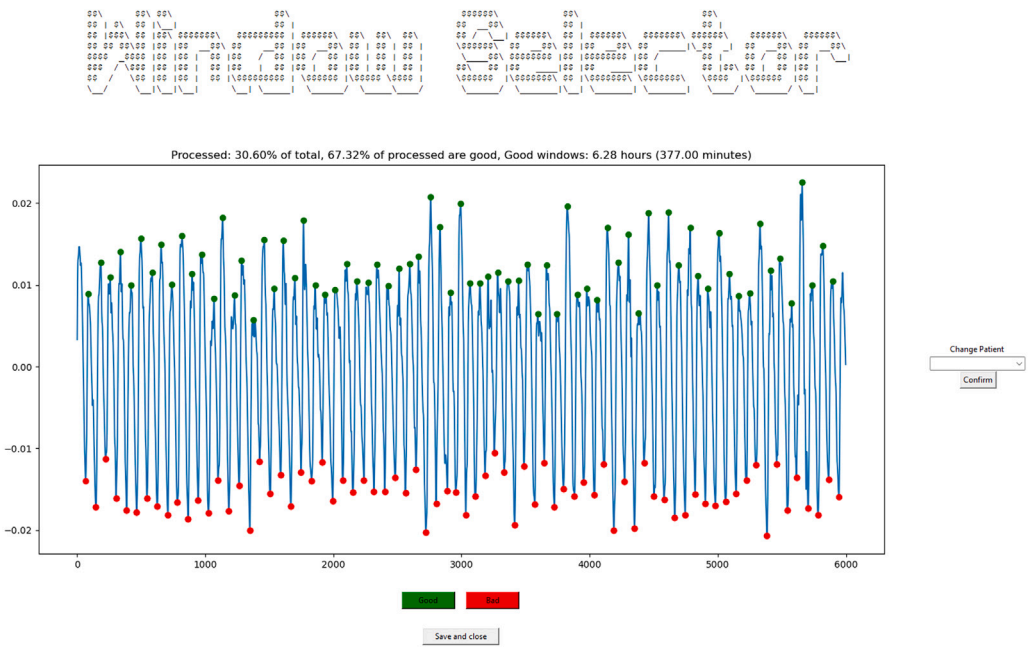

Fig. 7. A figure showcasing the *window selector* interface, illustrating a one-minute window of distal data. It displays the buttons provided for the user to categorise the data segment as "good" or "bad" quality. Additionally, the interface presents an overview at the patient level, indicating the volume of data analysed and the proportion of data classified as "good".

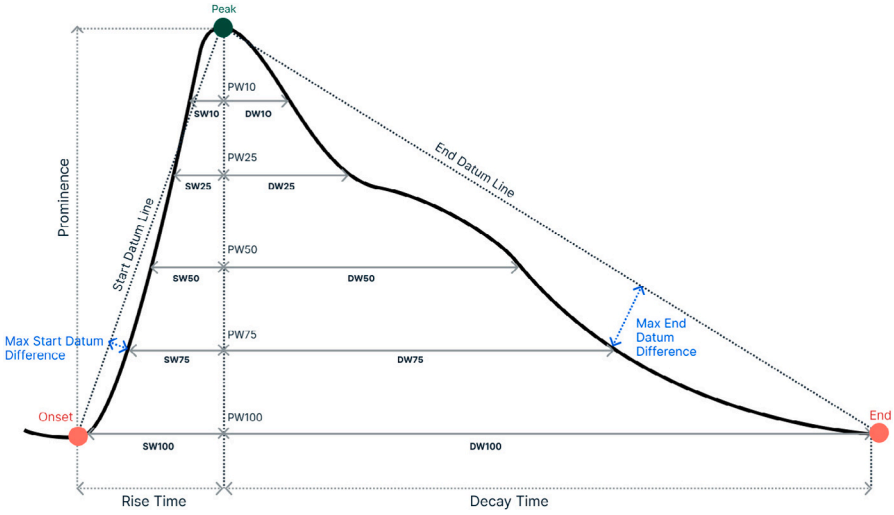

Fig. 8. A figure illustrating the key time-series and morphological features extracted from individual cardiac pulses. Within the figure, SW, DW, and PW represent systolic width, diastolic width, and pulse width, respectively. The numerical value associated with SW, DW, or PW indicates the position along the pulse prominence where the corresponding measurement is taken.

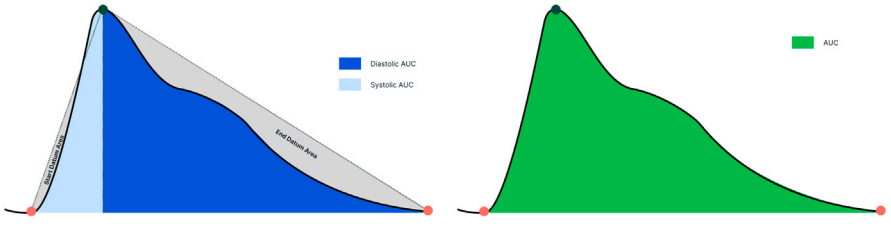

Fig. 9. A figure depicting the Area Under the Curve (AUC), along with the Diastolic AUC and Systolic AUC. Additionally, the start and end datum areas are identified.

points the location of the maximum value between crossing points is classified as a peak. Vice versa if the mean of the data between points is less than the mean of the moving average between crossing points the index of data which has the lowest value between points is classified as a trough. Once the peaks and troughs in the data have been identified, each peak is linked to its corresponding pulse onset and end in order to isolate each individual pulse. Fig. 10 illustrates and described the three major steps of the peak detection algorithm.

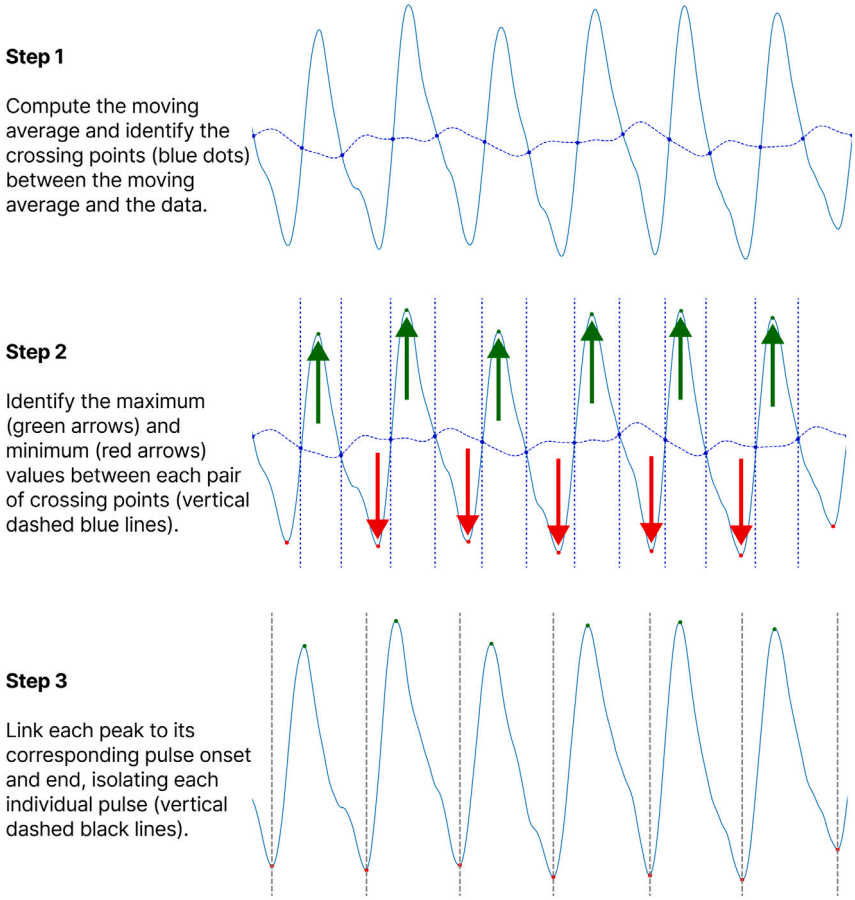

Fig. 10. This figure illustrates the major steps of the peak detection algorithm. The process begins with the calculation of the moving average and identification of the crossing points between the moving average and the raw data. Next, the algorithm determines the maximum and minimum values between each pair of crossing points, highlighted by green and red arrows, respectively. Finally, each detected peak is linked to its corresponding pulse onset and end, isolating individual pulses.

2.5. Statistical analysis

The study conducted two types of statistical analyses: correlation analysis and group analysis, to explore the two hypotheses of this study: (i) the relationship between alterations in NIR-PPG derived features and changes in ICP levels, and (ii) the comparative prominence of these changes in features obtained from long-distance versus short-distance NIR-PPG data. This analysis included data from both proximal and distal photodiodes, referred to as "proximal features" and "distal features", respectively.

To examine the relationship between individual features and the label, the Spearman correlation method was utilised. This choice was made over Pearson correlation as Spearman correlation is capable of identifying linear, non-linear, and non-monotonic relationships without assuming data linearity.

A group analysis was conducted to investigate the null hypothesis that there are no significant differences in feature values across ICP groups. For the group analysis, the study assessed the sampled feature data for normality using the Shapiro–Wilk Test and for homogeneity of variance using Levene's Test. If the data met the necessary assumptions, a parametric, One-way ANOVA was employed. If not, a Kruskal–Wallis non-parametric statistical test was applied. If a significant difference was detected for any feature in the across group analysis, a post hoc pairwise analysis was conducted to investigate the second null hypothesis that there are no significant differences in feature values between any two ICP groups. The post-hoc, pairwise analysis was conducted between groups using a Mann–Whitney U test with a Bonferroni correction to control for multiple comparisons.

2.5.1. Group construction and data sampling strategy

The group analysis necessitated the formation of groups and the sampling of data for each. Grouping started at an ICP of 0 mmHg, increasing in increments of 10 mmHg. If the highest recorded ICP value was above 20 mmHg and the gap between this maximum value and 20 mmHg exceeded 10 mmHg, an additional group was established, with its upper boundary set at this maximum ICP level.

The criteria for group formation specified that groups must span at least 10 mmHg to facilitate a meaningful comparison of feature variations across different ICP levels. This threshold was based on the premise that meaningful physiological changes are likely to be observed across ICP intervals exceeding 10 mmHg. Moreover, the larger group size allowed for the inclusion of data from more patients, especially in the underrepresented tails of the ICP distribution.

Elevated levels of ICP is referred to as intracranial hypertension which is typically defined as sustained ICP values greater than 20–25 mmHg [18]. Guidelines recommend treating elevated ICP above 22 mmHg [14]. An interest of this study was to examine feature changes across low, normal to moderate and elevated ICP values. In adults, normal ICP levels are typically between 10 to 15 mmHg [3]. The employed group construction methodology establishes reasonable bounds for low, normal to moderate, and high ICP ranges.

ICP dynamics vary between patients, particularly at the clinically scarce elevated ICP values. To strike a balance between the stratified sampling of patients' data and the power of the statistical test being conducted, a "bounded stratified sampling" approach was performed. The size of each group was determined based on the availability and eligibility of patient data within each group. Within each group, the

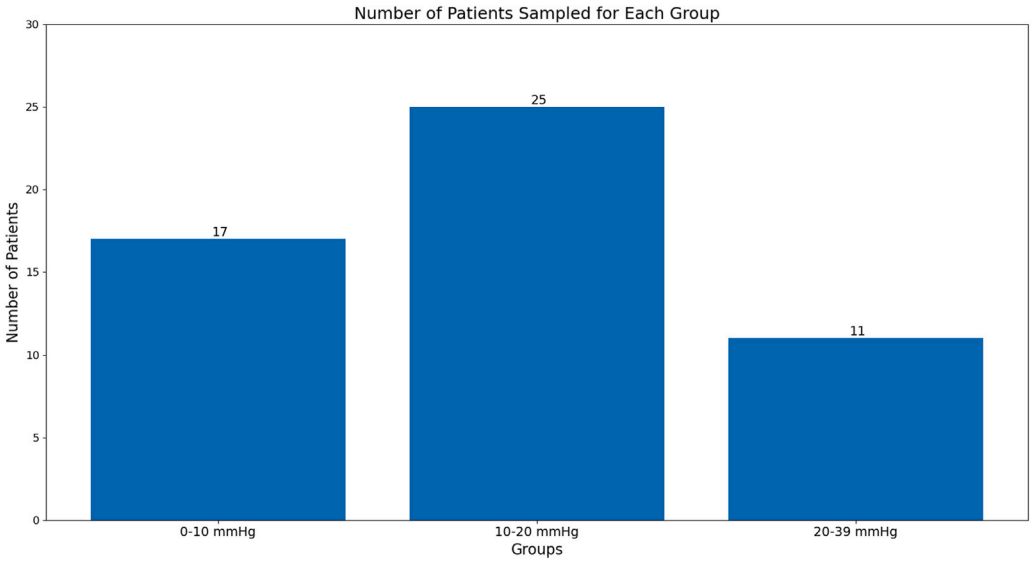

Fig. 11. This bar chart depicts the number of patients sampled for each intracranial pressure (ICP) group, categorised by the ranges of ICP values: 0–10 mmHg, 10–20 mmHg, and 20–39 mmHg. The chart highlights the distribution of patients within each group, with 17 patients in the 0–10 mmHg group, 25 patients in the 10–20 mmHg group, and 11 patients in the 20–39 mmHg group.

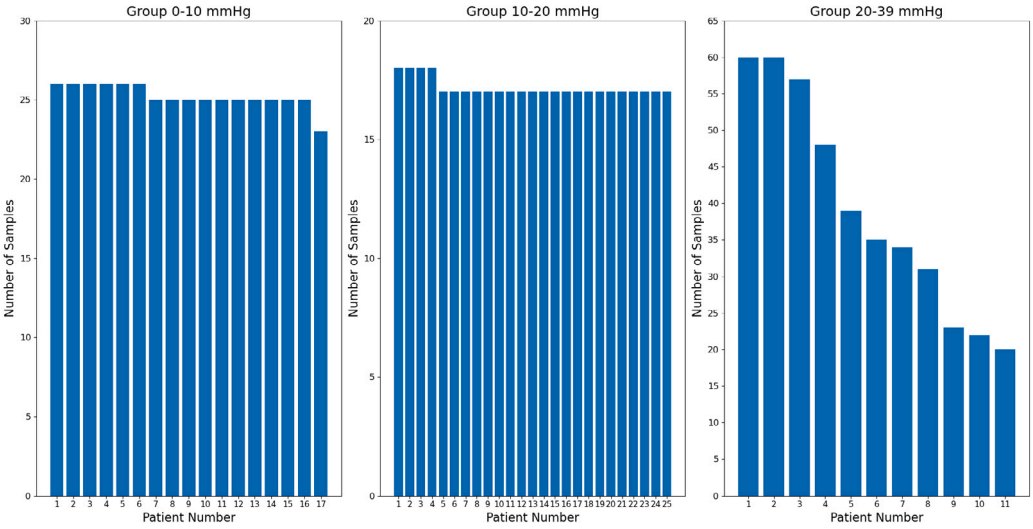

Fig. 12. A figure containing 3 bar charts depicting the number of samples collected from each patient within the defined ICP groups. The charts illustrate the distribution of samples across individual patients for the groups: 0–10 mmHg, 10–20 mmHg, and 20–39 mmHg.

number of data points available per patient was counted. To ensure meaningful statistical power and maintain a reasonable balance of representation between patients, only patients with a minimum of 20 data points (equivalent to 20 min of data) were considered eligible for sampling. The maximum number of samples that could be drawn from a single patient was limited to 60 data points, preventing any one patient from being disproportionately over-represented. The size of each group was then calculated by summing the contributions of eligible patients. To maintain consistency, the number of samples in each group was adjusted to match the size of the smallest group, ensuring uniformity in the analysis.

Once a group size had been defined, the sampling procedure involved iteratively and randomly drawing samples from the eligible patient data until the required number of samples for each group was reached. Figs. 11 and 12 depict the number of patients sampled for each group and the number of samples collected from each patient for each group, respectively.

3. Results

The findings affirm the two hypotheses under investigation, which we now examine sequentially. Initially, the outcomes from both the correlation and group analyses reinforce the hypothesis that variations in features derived from NIR-PPG correspond to changes in ICP levels. The correlation analysis revealed that the majority of the 141 features exhibited significant correlations ($p < 0.05$) with the label in both datasets. Notably, 109 (77.30%) and 112 (79.43%) of the features demonstrated significant correlations with the label for proximal and distal features, respectively. Table 1 presents the ten features with the smallest p-values for both proximal and distal feature sets. Due to the extensive number of features analysed, this discussion is concentrated on the top 10 most significant features, alongside aggregate metrics summarising the overall results.

For the significant features, the mean absolute correlation coefficients were 0.0729 and 0.0930 for proximal and distal features, respectively. Within the subset of the 10 most correlated features, these

Table 1
Table containing the top 10 correlated features sorted by ascending p-value for both short-distance, proximal and long-distance, distal NIR-PPG derived features. The Coefficient column represents the Spearman correlation coefficient, which ranges from −1 to 1. A value of 1 indicates a perfect positive correlation, −1 indicates a perfect negative correlation, and 0 indicates no correlation. Larger absolute values signify stronger relationships between features and the label.

Proximal		Distal	
Feature	Coefficient	Feature	Coefficient
start datum difference	−0.1943	ds ratio 75 (deriv 1)	−0.2149
max start datum difference	−0.1699	kurt	−0.2132
skew	0.1527	systolic width 50	−0.2064
systolic width 25 (deriv 2)	0.1499	diastolic width 75 (deriv 1)	−0.2051
ds ratio 75 (deriv 1)	−0.1472	ds ratio 50 (deriv 1)	−0.2051
pulse width 25 (deriv 2)	0.1466	skew	0.2038
kurt	−0.1337	ds ratio 75	0.2033
pulse width 50 (deriv 2)	0.1319	skew (deriv 1)	0.2003
ds ratio 75 (deriv 2)	−0.1276	pulse width 75 (deriv 1)	−0.2001
systolic width 25	−0.1275	ds ratio 50	0.1941

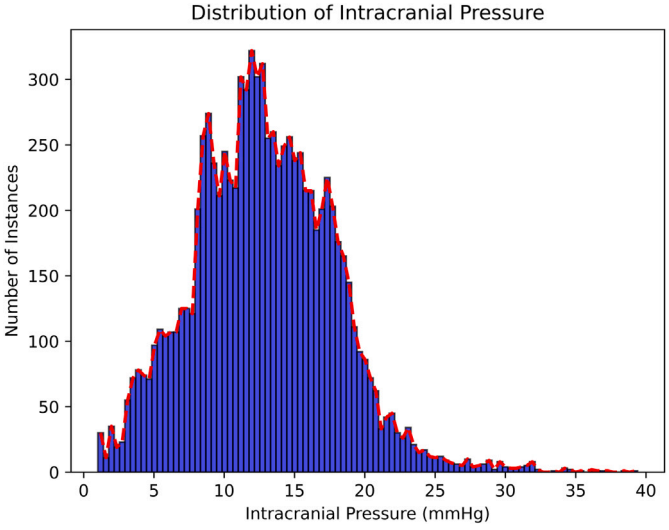

Fig. 13. A histogram illustrating the distribution of intracranial pressure values within the dataset.

averages increase to 0.1481 for proximal and 0.2046 for distal features. Excluding seven features (start datum difference, max start datum difference, skew, skew of the first derivative, and kurtosis) from the top 20 features across both proximal and distal datasets the remaining 65% of the features are related to pulse width.

The group analysis reinforces the findings of the correlation analysis and provides additional support for the initial hypothesis. The sampled data for all features did not meet the assumptions of normality and/or homogeneity of variance, as assessed by the Shapiro–Wilk and Levene's tests, respectively. Consequently a non-parametric Kruskal–Wallis test was employed to identify changes in the distributions of feature values across the ICP range. Fig. 13 illustrates the distribution of ICP values within the dataset.

The dataset's maximum ICP value was 39 mmHg. Following the logic for constructing groups, three groups were formed: (0–10), (10–20), and (20–39) mmHg. The smallest group, encompassing data from 20 to 39 mmHg, comprised 429 instances, equating to approximately 7.15 h of data. To ensure uniformity, the other groups were sampled to match this size. The results of the group analysis indicate that 115 (81.56%) and 107 (75.89%) features exhibited significant changes ($p < 0.05$) across ICP groups for proximal and distal features, respectively. Table 2 presents the top 10 features sorted by lowest p-value for both proximal and distal datasets.

Fig. 14 illustrates the top 10 distal features arranged by descending p-value returned by the Kruskal–Wallis analysis. The presented box plots provide a comparative analysis of feature values across ICP ranges for proximal (orange box plots) and distal (blue box plots) data. The presented box plots provide a comparative analysis of feature values across ICP ranges for proximal (orange box plots) and distal (blue box plots) data. Each box plot represents the distribution of a specific feature within a given ICP range. The boxes illustrate the interquartile range (IQR), containing the middle 50% of the data points. Inside each box, the red line indicates the median of the data, providing a measure of central tendency. The whiskers denote the range within 1.5 times the IQR from the quartiles. The box plots include annotations indicating the results of the overall group Kruskal–Wallis tests, which compare the distributions across different ICP groups. Additionally, the associated results of the post hoc pairwise analysis are annotated, indicating which pairs showed significant changes.

A visual examination of the boxplots indicate that the features derived from NIR-PPG data show statistically significant variations with changes in ICP. Across ICP groups, most of the examined features demonstrate significant changes in median values and IQR. Notably, the majority (approximately 60%) of the top 10 most significant features exhibit an inverse relationship with ICP, indicating that as ICP increases, the values of these features tend to decrease.

Focusing specifically on features within the top 10 that directly describe aspects of pulse width without referring to ratios of systolic to diastolic pulse widths, we observe consistent trends. Features such as the pulse width at 75% of pulse prominence (1st derivative), diastolic width at 50% of pulse prominence (1st derivative), and diastolic width at 75% of pulse prominence (1st derivative) all display a robust inverse relationship with ICP. These findings suggest that as ICP values rise, the width of the cardiac pulse decreases. Notably, the diastolic width emerges as one of the features undergoing the most significant changes, implying that the reduction in width may primarily stem from a decrease in the diastolic segment of the pulse.

Furthermore, along with the narrowing of pulse width, a significant relationship between skewness, kurtosis, and the ratio of diastolic to systolic width at different percentages of pulse prominence with ICP is observed. The observed decrease in kurtosis, increase in skew, and decrease in the ratio between the systolic and diastolic pulse width of the pulse may collectively indicate that the pulse is becoming more rounded. A decrease in kurtosis suggests that the pulse distribution is becoming less peaked and more flattened, implying a broader, more rounded shape. An increase in skew indicates a shifting or diminishing of the systolic peak, suggesting that the peak is either becoming less pronounced or moving away from the left hand side of the pulse, contributing to a more symetrical and rounded pulse shape. Additionally, a decrease in the ratio between the systolic and diastolic pulse

Table 2
Table containing the top 10 features which changed most significantly with variations in ICP values. The NIR-PPG derived features were sorted by ascending p-value for both short-distance, proximal and long-distance, distal data. The associated p-value and η^2 for each feature is also presented.

Proximal			Distal		
Feature	P-Value	η^2	Feature	P-Value	η^2
skew (deriv 1)	7.14E−37	0.128	skew (deriv 1)	1.04E−32	0.113
skew	7.51E−30	0.103	ds ratio 75 (deriv 1)	3.51E−30	0.104
ds ratio 75 (deriv 2)	7.20E−29	0.099	ds ratio 50 (deriv 1)	1.08E−28	0.099
ds ratio 50	9.15E−28	0.095	skew	6.61E−28	0.096
ds ratio 75	1.01E−25	0.088	diastolic width 75 (deriv 1)	1.15E−27	0.095
kurt	1.47E−25	0.088	kurt	1.09E−25	0.088
AUC Ratio	1.22E−24	0.084	diastolic width 50 (deriv 1)	1.30E−25	0.088
datum area ratio	8.40E−24	0.081	ds ratio 100	1.53E−25	0.087
end datum difference (deriv 1)	1.34E−23	0.080	pulse width 75 (deriv 1)	2.00E−25	0.087
ds ratio 100	5.76E−23	0.078	ds ratio 75	1.39E−24	0.084

indicates that the difference between these two phases is reducing, further supporting the idea that the pulse profile is losing its sharp systolic peak and becoming more uniformly rounded.

The majority (60%) of the top 10 features of the distal dataset which we posit includes cerebral information were first derivative features. The first derivative representing the velocity/rate of change over time. Within this context the first derivative may provide information about the velocity of blood volume changes happening within the cerebral vasculature.

A post hoc pairwise analysis was conducted using a Mann–Whitney U test with a Bonferroni correction if a significant change was detected across groups from the Kruskal–Wallis test. This approach led to the post hoc analysis of 115 and 107 features for the proximal and distal data, respectively.

In the proximal dataset, 80.87% and 86.09% of the features changed significantly between the 0–10 and 20–39 mmHg groups and the 10–20 and 20–39 mmHg groups, respectively. Similarly, in the distal dataset, 85.047% of features changed significantly between these same pairs. A minority of pairwise statistical changes were identified between the 0–10 mmHg and 10–20 mmHg groups. In the proximal and distal datasets, these changes accounted for 40% and 21.5%, respectively. These findings align with our expectation that the majority of features would show significant differences when comparing groups with low ICP (0–10 mmHg) and normal/moderate ICP (10–20 mmHg) to those with high ICP (20–39 mmHg).

The findings partially validate the second hypothesis, indicating that alterations in features are more prominent in long-distance NIR-PPG data compared to short-distance NIR-PPG data. Although there is a non-significant difference in the number of significantly correlated features (2.75%) and significant differences across groups (7.21%) between the proximal and distal datasets, the correlation analysis shows that the absolute average correlation coefficient of all features and significantly correlated features in the distal dataset is 25.76% and 24.24% higher, respectively, than in the proximal dataset. This suggests that distal, long-distance NIR-PPG pulse features may be more closely related to changes in ICP compared to proximal, short-distance features.

4. Discussion

4.1. Limitations

An important area for future research involves the collection of a new and more comprehensive dataset. The current dataset was limited by being a single-centre collection and included data from 27 patients after data exclusion. This relatively small sample size and the single-arm nature of the study poses possible limitations. A small sample size and single-centre study may limit the generalisability and reliability of the findings. Factors such as patient demographics and treatment protocols can vary significantly across different regions and centres. Data collected from a smaller sample from a single centre might not capture the variability seen in a more diverse, multi-centre study. Moreover, the dataset lacked stratified demographic and medical information, such as medication usage and skull thickness which could potentially serve as important features for non-invasive ICP estimation. Due to effective clinician intervention another limitation of the dataset was the scarcity of elevated and valuable ICP data above the clinically significant threshold of circa 20 mmHg.

An additional limitation of this study is the absence of MAP data and, consequently, autoregulation assessment. Without these data, the study did not explore the potential relationships and interactions between MAP, autoregulation, ICP, and changes in derived NIR-PPG features. Including MAP data and autoregulation assessment in future research would provide a more comprehensive view of the factors influencing ICP and their impact on NIR-PPG features, leading to an improved understanding of the underlying physiological mechanisms caused by variations in ICP and their effect on the NIR-PPG signal.

To address these challenges, a larger and multi-centre data collection would be useful to increase the sample size and diversity. A focus should be placed on collecting more data above the 20 mmHg threshold to possibly improve the robustness of the ICP estimation models and statistical analysis. A revised data collection protocol, which may involve shorter but more supervised collection periods, could help ensure higher data quality.

The developed pulse detection algorithm, tailored specifically for this dataset, was qualitatively assessed through visual inspection of the detection on NIR-PPG data during its development rather than through quantitative evaluation. We acknowledge that the absence of a quantitative assessment may lead to potential errors in pulse detection and subsequent feature extraction. However, we are reasonably assured of the accuracy of the extracted features for the included data. This assurance stems from the fact that the pulse detection algorithm's results were visually inspected and verified during the data selection process, as illustrated in Fig. 7. Thus, despite the potential limitations, we believe the qualitative assessment provided a satisfactory verification of the algorithm's performance for our purposes.

4.2. Findings and future directions

To the best of the authors' knowledge, this paper represents the first attempt to investigate variations in time-series and morphological features derived from NIR-PPG in response to changes in ICP, using clinically collected data from 27 patients. The initial hypotheses of this study were twofold: first, to ascertain whether alterations in NIR-PPG derived features correlate with fluctuations in ICP levels, and second, to determine whether these changes are more pronounced in features derived from long-distance NIR-PPG data compared to short-distance NIR-PPG data. The results of this investigation provide support for both hypotheses. The findings indicate that a majority of features derived from both short and long-distance NIR-PPG data exhibit significant changes in response to variations in ICP. Although there is a non-significant difference in the number of significantly correlated features

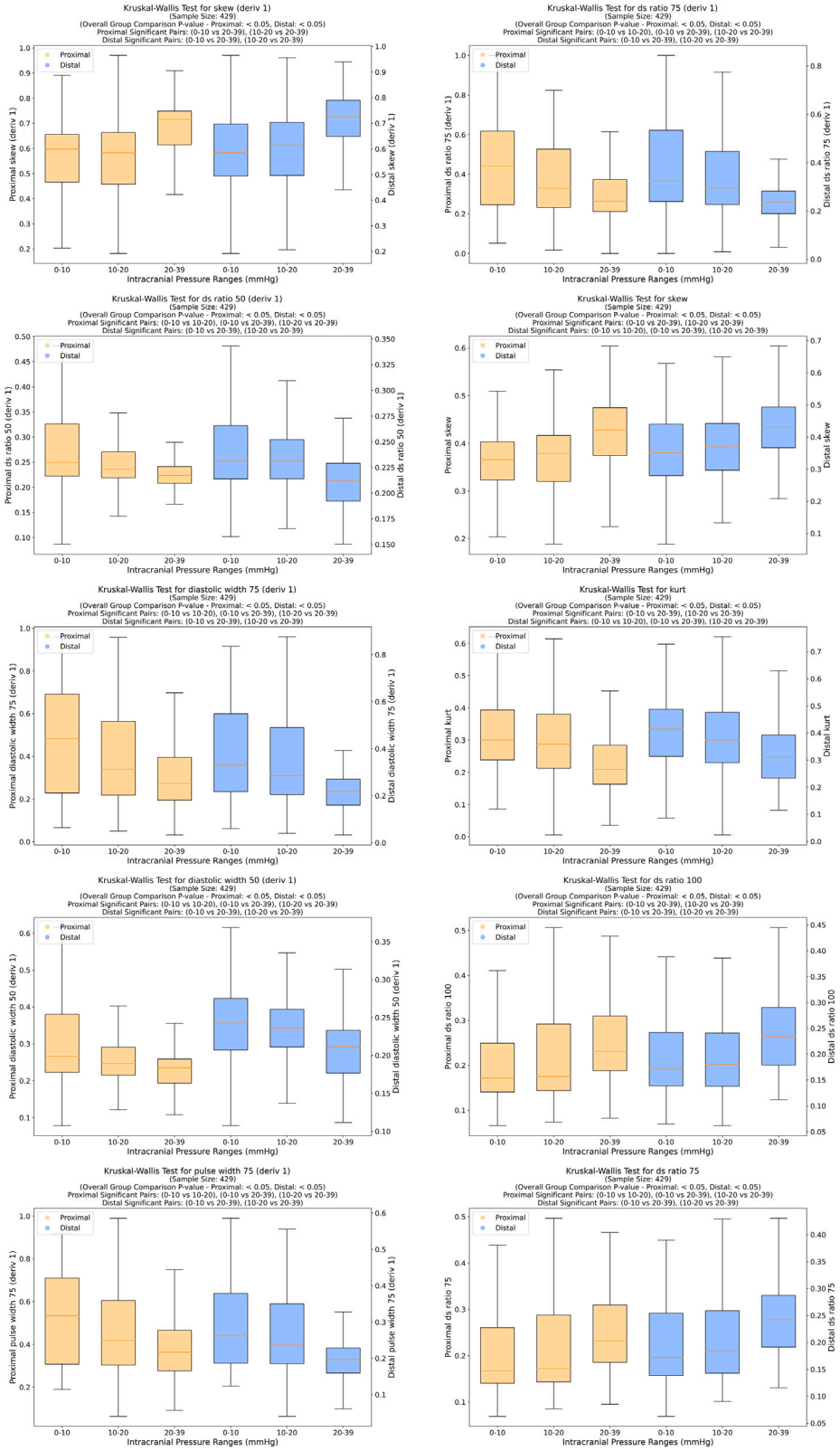

Fig. 14. A figure presenting 10 boxplots illustrating the variation in feature values across different ICP groups. These boxplots correspond to the 10 features with the most significant differences in a Kruskal–Wallis analysis on distal feature data. They display distributions for both proximal and distal feature data. The central line represents the median, the box encompasses the interquartile range (IQR), and the whiskers denote the range within 1.5 times the IQR from the quartiles.

and significant differences across groups between the proximal and distal datasets the distal dataset yielded a meaningfully higher absolute average correlation coefficient of all features and significantly correlated features in-comparison to the proximal dataset which supports the proposition by Roldan et al. that data from the proximal photodiode corresponds predominantly to extracerebral data, whereas data from the distal photodiode represents a combination of extracerebral and cerebral data [13].

In Section 1.1, we introduced our hypothesis regarding the relationship between cerebral hemodynamics and changes in NIR-PPG morphology. We describe how elevations in ICP correspond to compression of cerebral vessels altering their mechanical properties, causing a reduction in cerebral compliance, increase in vascular resistance and subsequent reductions in CPP. This process initiates cerebral autoregulatory mechanisms aimed at maintaining CPP and normalising CBF to the brain. However, when elevated ICP diminishes CPP below a critical threshold, cerebral autoregulation may fail, resulting in blood vessels being unable to vasodilate sufficiently to counter the reduced CPP, leading to a sustained drop in CBF. We contend that the NIR-PPG signal may offer insights into these variations in cerebral compliance and CBF. Our findings indicate that the majority of the most significant changes in distal features affected the pulse width. We hypothesise that the recorded changes in pulse width may reflect alterations in blood flow and vessel elasticity. As ICP increases, cerebral compliance decreases reducing CPP below the critical threshold and consequently diminishing CBF, less blood volume per cardiac cycle reaches the brain. We acknowledge that the normalisation of the NIR-PPG data prior to analysis does not enable us to determine if the changes in pulse width are as a consequence of shorter cycle duration or changes in amplitude. Despite this, we hypothesise a narrower pulse width may signify a shorter duration of blood volume change, potentially associated with decreased compliance or lower CBF. Decreased cerebral compliance may result in an increase in the velocity of blood volume changes due to the vessels' reduced ability to accommodate changes in blood volume, reducing the first derivative's pulse width.

The results also suggest that as ICP increases, pulses become more rounded, indicated by a decrease in kurtosis and the ratio of diastolic to systolic width at different percentages of pulse prominence coupled with an increase in skewness. This rounding of the pulse may also be associated with a dampening effect caused by reduced compliance. We posit that the diminished ability of vessels to deform during systole and diastole with decreased compliance attenuates the pulse wave creating the rounding effect.

The study conducted by Cardoso et al. [19] analysed the CBF pulse wave and its relationship with ICP in 15 patients suffering from hydrocephalus, benign intracranial hypertension or head injury. Our findings and hypothesis are in line with the outcomes of this study which found that increases in ICP is accompanied by an increase in the amplitude of the cerebrospinal fluid pulse wave which in values above 20 mmHg first become rounded and, at higher ICP values acquires a pyramidal shape.

Additionally, the majority of the most significant distal feature changes were observed in the first derivative, particularly within the distal dataset, which we believe encompasses cerebral information. The first derivative, representing flow velocity. An increase in ICP can compress cerebral vessels, thereby diminishing CBF. This constriction not only reduces the volume of blood that can flow through these vessels but may also affect the velocity of blood flow, likely captured by changes in the first derivative of the NIR-PPG signal. Consequently, a reduction in the width of the first derivative may signify a faster transit time of blood perhaps indicating compensatory mechanisms reacting to maintain cerebral perfusion under elevated ICP. Understanding these changes in features related to blood flow velocity appear crucial in describing ICP dynamics via NIR-PPG data.

The current study provides a credible foundation, but additional steps are required to develop this methodology into a clinically viable, non-invasive tool for estimating ICP. The next phase should involve collecting further data from a larger and more diverse patient population to enhance the robustness and generalisability of the findings.

This research has demonstrated that NIR-PPG features are associated with ICP changes, providing a basis for developing machine learning models. Effective models would enable non-invasive ICP monitoring and assessment. While NIR-PPG features derived from this dataset have demonstrated the feasibility of non-invasive ICP estimation using classical machine learning models, these models have struggled to generalise to new, unseen data [20]. Therefore, further research utilising more complex modelling approaches may improve ICP estimation performance. This research will contribute to the goal of the development of the first non-invasive, point-of-care device for ICP monitoring.

5. Conclusion

The results of this study support both hypotheses, demonstrating significant correlations between the extracted features and ICP levels. Significantly 77.30% and 79.43% of the features exhibited significant correlation with the label for the distal and proximal datasets, respectively. Moreover, the Kruskal–Wallis group analysis underscores the consistency of these findings, indicating that 81.56% and 75.89% of the features showcased significant changes across the ICP range. Notably, the mean absolute correlation of significant long-distance derived features surpassed short-distance features by 24.24%. These findings underscore the potential of NIR-PPG based devices as non-invasive tools for estimating dynamic changes in ICP. These findings are clinically relevant and support the work within this domain which strives to utilise NIR-PPG data and derived features to estimate ICP non-invasively providing a reference for demonstrating the sensitivity of NIR-PPG waveform features to alterations in ICP. The positive findings indicate promise in the area of NIR-PPG driven non-invasive ICP monitoring.

CRediT authorship contribution statement

George R.E. Bradley: Writing – review & editing, Writing – original draft, Visualization, Validation, Software, Methodology, Formal analysis, Data curation, Conceptualization. **Panicos A. Kyriacou:** Writing – review & editing, Supervision, Project administration, Methodology, Investigation, Funding acquisition, Conceptualization.

Declaration of competing interest

The authors declare that they have no known competing financial interests or personal relationships that could have appeared to influence the work reported in this paper.

Data availability

The data that has been used is confidential.

Acknowledgment

The study was financially supported by the George Daniel Doctoral Studentship at City University of London.

Appendix A

See Table 3.

Appendix B. Supplementary data

Supplementary material related to this article can be found online at https://doi.org/10.1016/j.bspc.2024.106759.

Table 3
Table containing the list of features extracted from the original, first derivative and second derivative of the signal.

Features
AUC
Systolic AUC
Diastolic AUC
Ratio between the systolic and diastolic AUC
Rise time (samples between the pulse onset and peak)
Decay time (samples between the pulse peak and end)
Ratio between the rise time and decay time
Number of beats
Inter-beat interval
Standard deviation of the inter-beat interval
Prominence
Upslope (slope between pulse onset to peak)
Downslope (slope between peak to pulse end)
Onset-end slope (slope between pulse onset and end)
Ratio between the upslope and downslope
Ratio between the pulse length and height
Start datum area (area between a straight line between the pulse onset and peak and pulse data between those points)
End datum area (area between a straight line between the pulse peak and end and pulse data between those points)
Ratio between the start datum area and end datum area
Max start datum difference (maximum element-wise difference between a straight line between the pulse onset and peak and pulse data between those points)
Max end datum difference (maximum element-wise difference between a straight line between the pulse peak and end and pulse data between those points)
The median of the element-wise difference between a straight line between the pulse onset and peak and pulse data between those points
The median of the element-wise difference between a straight line between the pulse peak and end and pulse data between those points
Pulse width at 10% of the pulse prominence (in samples)
Pulse width at 25% of the pulse prominence (in samples)
Pulse width at 50% of the pulse prominence (in samples)
Pulse width at 75% of the pulse prominence (in samples)
Pulse width at 100% of the pulse prominence (in samples)
Systolic width at 10% of the pulse prominence (in samples)
Systolic width at 25% of the pulse prominence (in samples)
Systolic width at 50% of the pulse prominence (in samples)
Systolic width at 75% of the pulse prominence (in samples)
Systolic width at 100% of the pulse prominence (in samples)
Diastolic width at 10% of the pulse prominence (in samples)
Diastolic width at 25% of the pulse prominence (in samples)
Diastolic width at 50% of the pulse prominence (in samples)
Diastolic width at 75% of the pulse prominence (in samples)
Diastolic width at 100% of the pulse prominence (in samples)
Ratio between the diastolic and systolic pulse width at 10% of the pulse prominence
Ratio between the diastolic and systolic pulse width at 25% of the pulse prominence
Ratio between the diastolic and systolic pulse width at 50% of the pulse prominence
Ratio between the diastolic and systolic pulse width at 75% of the pulse prominence
Ratio between the diastolic and systolic pulse width at 100% of the pulse prominence
Variance of the pulse data
Skew of the pulse data
Kurtosis of the pulse data
Zero-crossing rate of the pulse data

References

[1] O.B. Paulson, S. Strandgaard, L. Edvinsson, Cerebral autoregulation, Cerebrovasc. Brain Metab. Rev. 2 (2) (1990) 161–192.

[2] B. Mokri, The Monro-Kellie hypothesis: applications in CSF volume depletion, Neurology 56 (12) (2001) 1746–1748.

[3] L. Rangel-Castilla, S. Gopinath, C.S. Robertson, Management of intracranial hypertension, Neurol. Clin. 26 (2) (2008) 521–41, x.

[4] J. Moyle, Pulse Oximetry, 2nd Edn, BJA: Br. J. Anaesth. 89 (5) (2002) 802–803, http://dx.doi.org/10.1093/bja/89.5.802, arXiv:https://academic.oup.com/bja/article-pdf/89/5/802/696342/aef568.pdf.

[5] P. Kyriacou, J. Allen, Photoplethysmography: Technology, Signal Analysis and Applications, Elsevier Science, 2021, URL https://books.google.co.uk/books?id=d8wnEAAAQBAJ.

[6] A. Kampfl, B. Pfausler, D. Denchev, H.P. Jaring, E. Schmutzhard, Near infrared spectroscopy (NIRS) in patients with severe brain injury and elevated intracranial pressure, in: H.E. James, L.F. Marshall, H.J. Raulen, A. Baethmann, A. Marmarou, U. Ito, J.T. Hoff, T. Kuroiwa, Z. Czernicki (Eds.), Brain Edema X, Springer Vienna, Vienna, 1997, pp. 112–114.

[7] A. Ruesch, S. Schmitt, J. Yang, M.A. Smith, J.M. Kainerstorfer, Fluctuations in intracranial pressure can be estimated non-invasively using near-infrared spectroscopy in non-human primates, J. Cereb. Blood Flow Metabol. 40 (11) (2020) 2304–2314, http://dx.doi.org/10.1177/0271678X19891359, PMID: 31775565.

[8] A. Ruesch, J. Yang, S. Schmitt, D. Acharya, M.A. Smith, J.M. Kainerstorfer, Estimating intracranial pressure using pulsatile cerebral blood flow measured with diffuse correlation spectroscopy, Biomed. Opt. Express 11 (3) (2020) 1462–1476.

[9] F.A.J. Relander, A. Ruesch, J. Yang, D. Acharya, B. Scammon, S. Schmitt, E.C. Crane, M.A. Smith, J.M. Kainerstorfer, Using near-infrared spectroscopy and a random forest regressor to estimate intracranial pressure, Neurophotonics 9 (4) (2022) 045001.

[10] B. Dixon, J.M. Sharkey, E.J. Teo, S.A. Grace, J.S. Savage, A. Udy, P. Smith, J. Hellerstedt, J.D. Santamaria, Assessment of a Non-Invasive brain pulse monitor to measure Intra-Cranial pressure following acute brain injury, Med. Devices (Auckl) 16 (2023) 15–26.

[11] M. Roldan, G.R.E. Bradley, E. Mejía-Mejía, T.Y. Abay, P.A. Kyriacou, Non-invasive monitoring of intracranial pressure changes: healthy volunteers study, Front. Physiol. 14 (2023) 1208010.

[12] M. Roldan, P.A. Kyriacou, A non-invasive optical multimodal photoplethysmography-near infrared spectroscopy sensor for measuring intracranial pressure and cerebral oxygenation in traumatic brain injury, Appl. Sci. 13 (8) (2023) http://dx.doi.org/10.3390/app13085211, URL https://www.mdpi.com/2076-3417/13/8/5211.

[13] M. Roldan, S. Chatterjee, P.A. Kyriacou, Brain Light-Tissue interaction modelling: Towards a non-invasive sensor for traumatic brain injury, in: Annu Int Conf IEEE Eng Med Biol Soc, vol. 2021, 2021, pp. 1292–1296.

[14] N. Carney, A.M. Totten, C. O'Reilly, J.S. Ullman, G.W.J. Hawryluk, M.J. Bell, S.L. Bratton, R. Chesnut, O.A. Harris, N. Kissoon, A.M. Rubiano, L. Shutter, R.C. Tasker, M.S. Vavilala, J. Wilberger, D.W. Wright, J. Ghajar, Guidelines for the management of severe traumatic brain injury, fourth edition, Neurosurgery 80 (1) (2017) 6–15.

[15] J. Murkin, M. Arango, Near-infrared spectroscopy as an index of brain and tissue oxygenation, Br. J. Anaesth. 103 (2009) i3–i13.

[16] G.R.E. Bradley, P.A. Kyriacou, Opening the envelope: Efficient envelope-based PPG denoising algorithm, 2023, Manuscript (submitted for publication).

[17] H. Adams, J. Donnelly, M. Czosnyka, A.G. Kolias, A. Helmy, D.K. Menon, P. Smielewski, P.J. Hutchinson, Temporal profile of intracranial pressure and cerebrovascular reactivity in severe traumatic brain injury and association with fatal outcome: An observational study, PLOS Med. 14 (2017) 1–21, http://dx.doi.org/10.1371/journal.pmed.1002353.

[18] J. Ghajar, Traumatic brain injury, Lancet 356 (9233) (2000) 923–929.

[19] E.R. Cardoso, J.O. Rowan, S. Galbraith, Analysis of the cerebrospinal fluid pulse wave in intracranial pressure, J. Neurosurg. 59 (5) (1983) 817–821.

[20] G.R. Bradley, P.A. Kyriacou, Evaluating the effectiveness of non-invasive intracranial pressure monitoring via near-infrared photoplethysmography using classical machine learning methods, Biomed. Signal Process. Control 96 (2024) 106517, http://dx.doi.org/10.1016/j.bspc.2024.106517, URL https://www.sciencedirect.com/science/article/pii/S1746809424005755.